Crystalline structure and optical spectroscopy of Er^{3+}-doped KGd(WO$_4$)$_2$ single crystals

M.C. Pujol[1], **M. Rico**[2], **C. Zaldo**[2,*], **R. Solé**[1], **V. Nikolov**[3], **X. Solans**[4], **M. Aguiló**[1], **F. Díaz**[1]

[1] Laboratori de Física Aplicada i Cristallografia, Universitat Rovira i Virgili, 43005 Tarragona, Spain
[2] Instituto de Ciencia de Materiales de Madrid, Consejo Superior de Investigaciones Científicas, Cantoblanco, 28049 Madrid, Spain
[3] Institute of General and Inorganic Chemistry, Bulgarian Academy of Sciences, 1113 Sofia, Bulgaria
[4] Departament de Cristallografia i Mineralogia, Universitat de Barcelona, 08028 Barcelona, Spain

Abstract. KGd(WO$_4$)$_2$ single crystals doped with Er^{3+} have been grown by the flux top-seeded-solution growth method. The crystallographic structure of the lattice has been refined, being the lattice constants $a = 10.652(4)$, $b = 10.374(6)$, $c = 7.582(2)$ Å, $\beta = 130.80(2)°$. The refractive index dispersion of the host has been measured in the 350–1500 nm range. The optical absorption and photoluminescence properties of Er^{3+} have been characterised in the 5–300 K temperature range. At 5 K, the absorption and emission bands show the $(2J+1)/2$ multiplet splittings expected for the C_2 symmetry site of Er in the Gd site. The energy positions and halfwidths of the 72 sublevels observed have been tabulated as well as the cross sections of the different multiplets. Six emission band sets have been observed under excitation of the $^4F_{7/2}$ multiplet. The Judd–Ofelt (JO) parameters of Er^{3+} in KGW have been calculated: $\Omega_2 = 8.90 \times 10^{-20}$ cm^2, $\Omega_4 = 0.96 \times 10^{-20}$ cm^2, $\Omega_6 = 0.82 \times 10^{-20}$ cm^2. Lifetimes of the $^4S_{3/2}$, $^4F_{9/2}$, and $^4I_{11/2}$ multiplets have been measured in the 5–300 K range of temperature and compared with those calculated from the JO theory. A reduction of the $^4S_{3/2}$ and $^4I_{11/2}$ measured lifetimes with increasing erbium concentration has been observed, moreover the presence of multiphonon non-radiative processes is inferred from the temperature dependence of the lifetimes.

PACS: 78.55.Hx; 42.70.Hj; 42.55.Rz

The technological interest in the development of solid-state lasers for application in long-distance optical communications has promoted the study of laser ions with an emission close to the minimum of the optical losses in silica fibers, namely 1.5 μm. In this respect, an extensive study of the Er^{3+} spectroscopic properties in glasses [1] and crystals, YVO$_4$ [1]; Y$_3$Al$_5$O$_{12}$, YAlO$_3$, Gd$_3$Ga$_5$O$_{12}$, Gd$_3$Sc$_2$Ga$_3$O$_{12}$ [2], LiNbO$_3$ [3, 4] and other lattices [5] has been undertaken, since the $^4I_{13/2} \rightarrow {}^4I_{15/2}$ erbium emission lies in this spectral region. Further interest in erbium lasers

arises from the ≈ 2.8 μm ($^4I_{11/2} \rightarrow {}^4I_{13/2}$) erbium emission for medical uses [2, 6].

The present development of a new laser generation requires us to find crystals with low excitation threshold and suited to be excited by the emission of diode lasers. Er^{3+} only has weak absorption bands in the 600–1000 nm region, but its photoluminescence can be sensitised by energy transfer from Yb^{3+}, which shows a strong optical absorption in the 900–1000 nm range. This region overlaps the emission of InGaAs diode lasers. As a matter of fact, InGaAs diode-pumped room-temperature laser operation has been recently demonstrated in KGd(WO$_4$)$_2$:Yb:Er crystals [7] (hereafter KGd(WO$_4$)$_2$ is abbreviated as KGW), however the efficiency of the process was weak and the physical processes involved were poorly understood. Moreover, Er has been used to sensitise the Tm^{3+} emission in KGW crystals at liquid nitrogen temperature [8].

Despite the relevance of the optical properties of Er^{3+} in KGW crystals, its spectroscopic properties have been reported at 77 K only for the $^4S_{3/2}$ or lower energy levels [9, 10]. The present work reports a spectroscopic study of the Er^{3+} ions incorporated in KGW crystals grown by the flux top-seeded-solution growth (TSSG) technique.

KGW crystals have been also used as a laser host for Nd^{3+} ions because of the high efficiency of the $^4F_{3/2} \rightarrow {}^4I_{11/2}$ transition [11, 12] as well as a host for other rare-earth laser ions [8]. Recently, some research has focused attention on crystals with relevant cubic nonlinearity $\chi^{(3)}$ because with these materials it is possible to obtain unconventional lasers, such as lasers with stimulated-Raman-scattering (SRS) frequency self-conversion. The KGW:Nd possesses an effective cubic nonlinearity of about 10^{-13} esu and presents a good efficiency in the process of SRS self-conversion [13].

In view of the relevance of the KGW lattice host, we have also performed a refinement of the crystal structure, in order to improve the currently known lattice constants and to help in the discussion of the local lattice site symmetry when required. Further, we discuss the orientation of the indicatrix of the crystal with regards to the crystallographic axes and we have obtained the value of the refractive indices in a wide spectral region.

* Corresponding author. E-mail: cezaldo@icmm.csic.es

1 Crystal growth

Inclusion-free $KGd_{1-x}Er_x(WO_4)_2$ single crystals were grown by the TSSG slow-cooling technique, using $K_2W_2O_7$ as solvent. The solution composition was $88.5\,K_2W_2O_7$-$11.5\,KGd_{1-x'}Er_{x'}(WO_4)_2$ molar ratio, with $x' = 0.01$, 0.03, and 0.05.
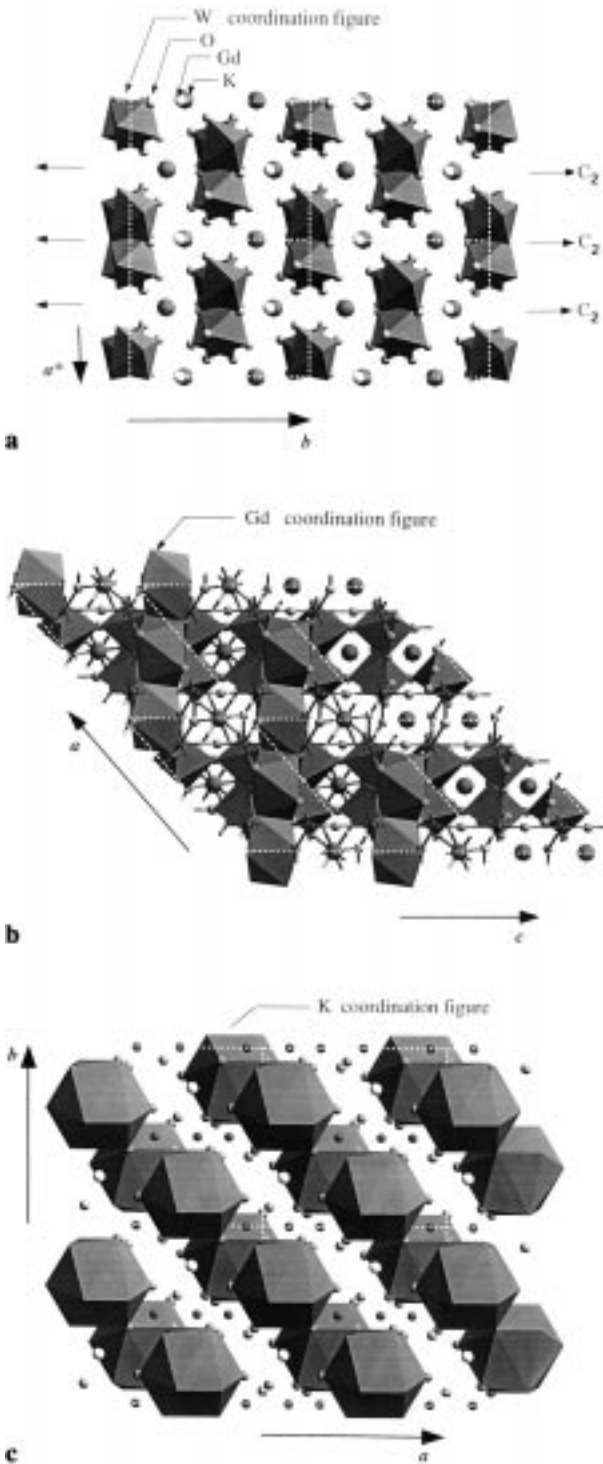

Fig. 1a–c. Projections of $KGd(WO_4)_2$ crystalline structure: **a** Parallel to the **c** direction, **b** parallel to the **b** direction, **c** parallel to the **c*** direction

The solutions used in the crystal growth experiments, weighing about 195 g, were prepared in a cylindrical Pt crucible, 50 mm in diameter, by melting and decomposing the appropriate quantities of K_2CO_3, Gd_2O_3, Er_2O_3, and WO_3. The axial difference of temperature in the solution was about 5 °C (hot bottom), while the radial one was about 2 °C (hot crucible wall). The homogenisation of the solutions was achieved by maintaining them at about 50 °C above the expected saturation temperature (T_{sat}) for 5–6 h. Afterwards, T_{sat} was more accurately determined by observing the growth/dissolving of a seed located at the centre of the free surface of the solution. After that, the growth process began in air on the **b**-oriented seed by reducing the temperature at a rate of 0.1 °C/h for the first 2 °C and 0.05 °C/h for the next 8.5 °C. During the growth, the seed was rotating at 60 rpm, without pulling.

After eight days of growth, the crystals were removed slowly from the solution and cooled to room temperature at 15 °C/h in order to avoid thermal shocks. The typical dimensions of the crystals grown were 10–12 mm × 5 mm × 14–17 mm along the **a*** (reciprocal axis, see Fig. 1), **b**, and **c** directions, respectively, with a weight of about 3.5–4 g (average growth rate ≈ 0.5 g/day). More details on the crystal growth can be found elsewhere [14]. The substitution level of Gd^{3+} by Er^{3+} in the crystals was tested by EPMA (electron probe microanalysis), using a Cameca Camebax SX 50 equipment. The atomic erbium concentrations obtained in the crystals were $5 \times 10^{19}\,cm^{-3}$, $15 \times 10^{19}\,cm^{-3}$, and $24 \times 10^{19}\,cm^{-3}$ for the three doping cases mentioned above, $KGd_{1-x}Er_x(WO_4)_2$ ($x = 0.008$, 0.024, and 0.04) being the corresponding stoichiometric formulas. These values would lead to a distribution coefficient $K_{Er} = 0.8$[1] for all the cases considered in the present work. It must be noted that these concentrations have a high uncertainty due to the overlap between the X-ray emissions of Gd^{3+} and Er^{3+} ions. The erbium concentration in the lowest concentrated sample, used later for the calculation of the optical absorption oscillator strengths, was further analysed by particle-induced X-ray emission (PIXE). The erbium concentration obtained was $1.1 \times 10^{20}\,cm^{-3}$. This is about twice the concentration obtained by EPMA, which provides an estimation of the uncertainty in the erbium concentration determination. We will use this latter erbium concentration because it provides a better agreement with previous spectroscopic results of Er^{3+} in other materials.

2 Crystal structure

The KGW crystal structure has been obtained and refined by using precise X-ray diffractometry data performed on spherical-shaped crystalline samples with a diameter of 0.40(2) mm, mounted on an Enraf–Nonius CAD4 four-circle diffractometer. The crystal structure of $KGd(WO_4)_2$ is monoclinic with space group $C2/c$. The lattice parameters of the unit cell obtained in the present work are, $a = 10.652(4)$, $b = 10.374(6)$, $c = 7.582(2)$ Å, $\beta = 130.80(2)°$ ($V = 634.2(5)\,Å^3$), and $Z = 4$. The atomic coordinates of the unit cell, the atomic effective thermal oscillations and

---

[1] $K_{Er} = \dfrac{(\text{moles Er}/(\text{moles Er} + \text{moles Gd}))_{\text{crystal}}}{(\text{moles Er}/(\text{moles Er} + \text{moles Gd}))_{\text{solution}}}$

Table 1. Coordinates of basic atoms and their thermal oscillation parameters (U_{ij}). U(eq) is defined as one third of the trace of the orthogonalized U_{ij} tensor

Atom	Crystallographic position Symmetry *	Multiplicity **	x/a	y/b	z/c	U(eq)	U_{11}	U_{22}	U_{33}	U_{23}	U_{13}	U_{12}
Gd	2 C_2	4	0	0.7277(1)	0.2500	0.013(1)	0.015(1)	0.013(1)	0.014(1)	0	0.010(1)	0
W	1 C_1	8	0.1949(1)	−0.0001(1)	0.7359(1)	0.013(1)	0.015(1)	0.013(1)	0.014(1)	0.000(1)	0.010(1)	0.000(1)
K	2 C_2	4	0.5000	0.2000(3)	0.7500	0.017(1)	0.018(1)	0.018(1)	0.016(1)	0	0.012(1)	0
O(1)	1 C_1	8	0.3726(14)	−0.0741(12)	0.8106(18)	0.046(2)	0.060(7)	0.039(5)	0.048(5)	−0.003(5)	0.039(5)	−0.003(5)
O(2)	1 C_1	8	0.0258(14)	−0.1090(12)	0.4713(17)	0.045(2)	0.056(6)	0.040(5)	0.046(5)	0.001(4)	0.036(5)	−0.001(4)
O(3)	1 C_1	8	0.2690(13)	0.1593(12)	0.8686(17)	0.045(2)	0.051(6)	0.044(5)	0.044(5)	0.000(4)	0.033(5)	−0.001(5)
O(4)	1 C_1	8	0.1905(14)	−0.0749(12)	0.9381(18)	0.044(2)	0.055(6)	0.044(5)	0.043(4)	0.000(5)	0.037(5)	0.002(5)

  * Hermann-Mauguin nomenclature
** Schöenfliess nomenclature

Table 2. Principal inter-atomic distances. # Equivalent atoms by symmetry transformations of the space group

Atoms	Distance /Å
Gd−O(2)#1	2.271(12)
Gd−O(2)#2	2.271(12)
Gd−O(1)#3	2.325(12)
Gd−O(1)#4	2.325(12)
Gd−O(3)#5	2.371(10)
Gd−O(3)#6	2.371(10)
Gd−O(3)#7	2.650(11)
Gd−O(3)#8	2.650(11)
W−O(4)	1.747(10)
W−O(1)	1.758(12)
W−O(3)	1.825(12)
W−O(2)	1.955(11)
W−O(2)#10	2.109(11)
W−O(4)#11	2.359(9)
K−O(4)#14	2.796(13)
K−O(4)#6	2.796(13)
K−O(4)#11	2.821(12)
K−O(4)#12	2.821(12)
K−O(1)#11	2.956(11)
K−O(1)#12	2.956(11)
K−O(2)#6	3.038(12)
K−O(2)#14	3.038(12)
K−O(3)	3.152(11)
K−O(3)#15	3.152(11)
K−O(1)	3.309(12)
K−O(1)#15	3.309(12)
Gd−W#7	3.549(2)
Gd−W#8	3.549(2)
Gd−K#5	3.8018(10)
Gd−K#9	3.8018(10)
W−K#12	3.675(2)
W−K#13	3.780(3)
W−K	3.798(2)

the symmetry and multiplicity of their crystallographic positions are summarised in Table 1. Table 2 summarises the interatomic distances in the lattice. W and O atoms, being in the 1.747–2.359 Å distance range, are the shortest pairs in the structure and form stable WO_4^{2-} octahedral anionic complexes sharing edges. The structure shows that the resulting octahedra constitute a double chain extended along the c axis by linking octahedra with common vertices. The K$^+$ and Gd^{3+} cations occupying C_2 symmetry positions, as is indicated in Fig. 1a. The coordination number of Gd^{3+} cations

is 8 and this coordination depicts square antiprism polyhedra which configure a single chain extended along the [101] direction, as shown in Fig. 1b. Finally, the K$^+$ cations present a distorted icosahedral coordination with 12 neighbours forming chains along the [$\bar{1}$10] direction, see Fig. 1c.

These structural results are in a good agreement with those published for KY(WO$_4$)$_2$ isomorphous substance [8, 15]. Other authors have published different unit cell parameters [7, 11, 13, 16], but sometimes non-equivalents. Our present results are equivalent to $a' = 7.582$ Å, $b' = 10.374$ Å, $c' = 8.087$ Å, $\beta' = 94.41°$ only if the space group $I2/a$ was assumed. In this case the axes transformation would be $a' = c$, $b' = b$, $c' = -(a+c)$. However the selection of the $C2/c$ space group is recommended as standard setting [17], of course with their corresponding a, b, c, β parameters.

Er^{3+} in KGW occupies the same position as Gd^{3+}. For the Er concentrations used in this work ($x < 0.04$), the crystalline structure of KGd$_{1-x}$Er$_x$(WO$_4$)$_2$ does not change, so the crystals optically studied in the present work have the same symmetry and only a slight change in the cell parameters is observed as a consequence of the different ionic radii of Gd^{3+} and Er^{3+}. This produces a reduction of about 0.15% in the cell volume.

3 Optical properties

3.1 Refractive indices

KGW is a biaxial crystal whose linear optical properties are described by the $2/m$ crystallographic point group. One of the principal axis is parallel to the b axis and the corresponding refractive index is labelled as n_p being the smallest one of the three independent refractive indices. Due to the selection of some different unit cells, there is some uncertainty in the published work on the refractive index values and orientation of the indicatrix, moreover the refractive index measurements available to date are limited to $\lambda = 1.06$ μm.

In order to determine the orientation of the indicatrix with regards to the crystallographic axes we have performed reflectance measurements at normal incidence with vertically polarised light. In this configuration the reflectivity, r, takes the simple expression, $r = (n-1)^2/(n+1)^2$. To this purpose a (010)-oriented parallel plate was rotated around the b axis, taking the crystallographic a and c axes as reference. The back side of the slab had a rough finishing in order to minimise the internal reflections. The reflected light intensity

showed an oscillatory behaviour and the maxima and minima allow us to determine the position of the two principal axes in the (010) plane. The principal axis with maximum refractive index, n_g, was found at $21.5° \pm 1°$ of the c axis in the clockwise rotation direction when looking opposite to the b axis. Finally, the principal axis with intermediate refractive index, n_m, was found orthogonal to the n_g axis. The orientation of the principal axes with regards to the crystallographic ones is illustrated in the inset of Fig. 2. In this inset the position of the c' axis referred above is also included to ease the comparison.

The crystal morphology helps to determine the position of the n_g and n_m axes. The crystals grown from b-oriented seeds shows the c axis in the direction of largest dimension and the [101] axis as a natural edge, this edge being tilted with regards to the c axis by $85.59°$ in the anti-clockwise rotation direction depicted in the inset of Fig. 2 (note that the angle stated as $85.59°$ in Fig. 2 of our previous work [14] must be $94.41°$). Therefore, the principal axis corresponding to the n_g refractive index may be roughly found identifying the c axis by inspection and rotating $21.5°$ in the direction of the largest angle formed by the [101] sample edge and the c axis.

Figure 2 shows the dispersion of the refractive indices in the visible and near-infrared regions. The indices have been determined by the minimum deviation angle using three different KGW prisms, each one cut perpendicularly to a principal axis. The accuracy of the refractive index determination is 0.001. The refractive index variations have been described by an infrared-corrected Sellmeier law:

$$n = A + \frac{B}{1 - \left(\frac{C}{\lambda}\right)^2} - D\lambda^2. \tag{1}$$

Table 3 summarises the A, B, C, and D parameters obtained from the best fits of the experimental results. The refractive indices measured at $\lambda = 1.06\,\mu m$, agree well which those given by Graf et al. [18], however those reported by Mochalov [13] and often used in the literature are lower than those obtained in our samples. The angle between the optical axes of KGW calculated from the refractive index values
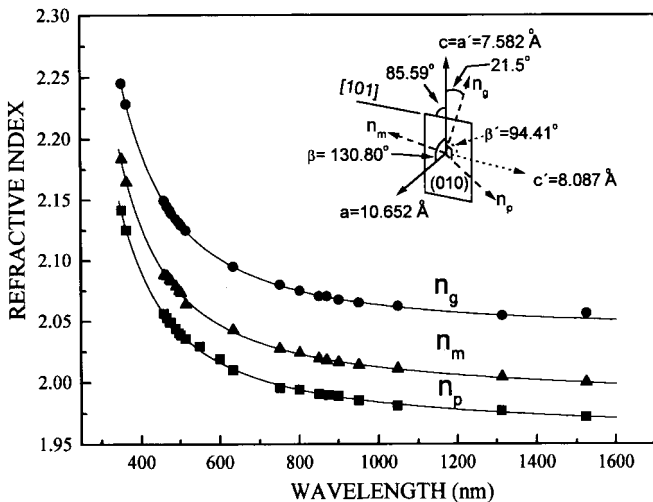
Table 3. Sellmeier parameters of the room-temperature refractive indices of undoped KGW crystals

	A	B	C/nm	D/nm^{-2}
n_g	1.3867	0.6573	170.02	0.2913×10^{-9}
n_m	1.5437	0.4541	188.91	2.1567×10^{-9}
n_p	1.5344	0.4360	186.18	2.0999×10^{-9}

obtained is in the 80–70° range for the 350–1300 nm spectral region. This is in any case lower than the value obtained previously by goniometric measurement, namely 86.5° [19].

3.2 Optical absorption

The unpolarized optical absorption studies were performed on plates cut perpendicular to the b axis using a diamond saw. These plates were oriented by X-ray diffraction technique and polished to optical quality using diamond powders.

The low-temperature optical absorption spectra were collected using a Varian spectrophotometer model 5E. The samples were cooled in an Oxford cryostat and the temperature was controlled with a Lake Shore model DRC 91C apparatus.

Figure 3 shows the relevant portions of the unpolarized optical absorption spectra of Er^{3+} in KGW at room temperature (RT) and 5 K. The different band sets presented have
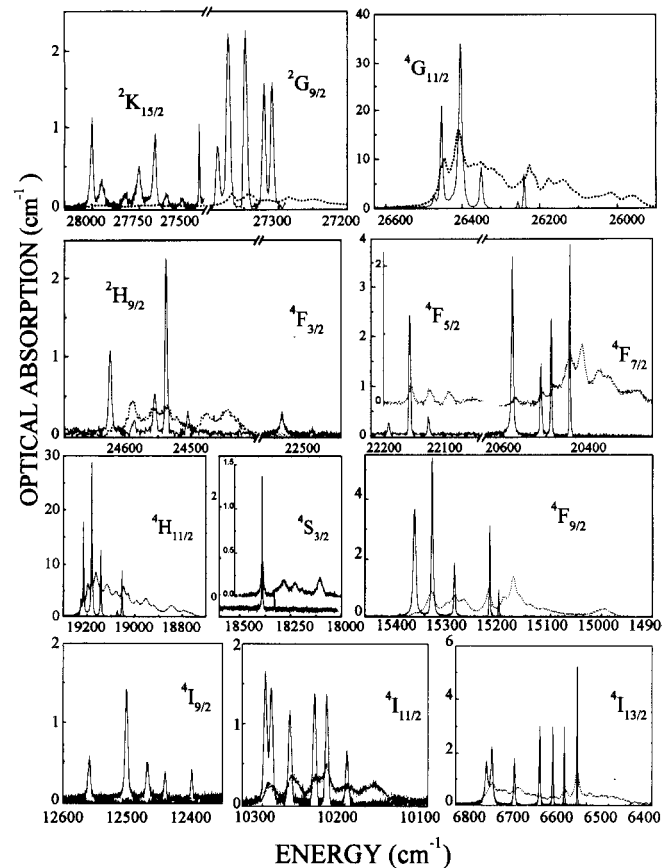

Fig. 2. Wavelength dependence of the refractive indices of $KGd(WO_4)_2$ crystals at 300 K. The *continuous lines* are the Sellmeier fits obtained with the parameters reported in Table 3. The inset shows the sample morphology and the orientation of the principal and crystallographic axes

Fig. 3. Unpolarized optical absorption of Er^{3+} in $KGd(WO_4)_2$ single crystals measured at 5 K (*solid lines*) and 300 K (*dotted lines*). [Er] = 1.1×10^{20} cm^{-3}. Some of the spectra at 300 K have been shifted in the y axis for clarity

been labelled according to the expected positions found in other lattice hosts [1–6]. The Er^{3+} bands appear well resolved at 5 K but at RT these bands become broader and overlapped. This behaviour is related to the thermal population of the ground multiplet sublevels and to the phonon-assisted transitions.

The $2J + 1$ free ion degeneracy of the $^{2S+1}L_J$ multiplets is reduced by the crystal field giving rise to Stark sublevels. The odd electron number of the $4f^{11}$ Er^{3+} electron configuration and the local C_2 symmetry surrounding the Er^{3+} position lead to Kramers-degenerated doublets. The energy positions, E_i, of the Stark sublevels with regards to the ground one are summarised in Table 3, as well as the mean position of each multiplet, $\overline{E} = (\sum_i E_i \Gamma_i / \sum_i \Gamma_i)$, where Γ_i is the integrated absorption of each Stark sublevel. Figure 4 sketches the energy position of the multiplets. This degeneracy is in very good agreement with the presence of $(2J + 1)/2$ components in each one of the absorption band sets observed.

The integrated absorption cross section, $\int_{JJ'} \sigma(\lambda) \, d\lambda$, for each JJ' (J being the fundamental multiplet) band of the Er^{3+} in KGW have been obtained from the integrated absorbance, $\Gamma_{JJ'} = \int \alpha(\lambda) \, d\lambda$, and the impurity density, N, as $\int \sigma(\lambda) \, d\lambda = \Gamma_{JJ'}/N$. The results obtained are shown in Table 4. It is worth noting that the absorption cross section of most of the multiplets increases with increasing temperature. As a consequence of the mixing of the electronic levels with vibration lattice modes the transition becomes most allowed. Some exceptions to this behaviour are the $^4I_{11/2}$ and $^4F_{5/2}$ levels.

The room-temperature optical absorption and photoluminescence properties of rare-earth ions can be described using the Judd–Ofelt (JO) theory [20, 21]. The experimental oscillator strengths, f_{exp}, can be can calculated according to the expression

$$f_{exp} = \frac{2mc}{\alpha_f h N \overline{\lambda}^2} \Gamma_{JJ'} \qquad (2)$$

where m is the electron mass, c the vacuum speed of the light, α_f the fine-structure constant, h Planck's constant, and $\overline{\lambda}$ is the average wavelength of the $J \to J'$ transition. In erbium these values can be identified with the electric dipolar oscillator strengths with the exception of that corresponding to the $^4I_{15/2} \to {}^4I_{13/2}$ transition for which the magnetic dipolar contribution has to be discounted. This contribution can be calculated as

$$f_{MD, th} = \frac{nh}{6mc\overline{\lambda}(2J+1)}$$
$$\times |\langle 4f^N \alpha[SL]J \parallel L + 2S \parallel 4f^N \alpha'[S'L']J' \rangle|^2, \quad (3)$$

where n is the refractive index. The expressions of the reduced matrix elements $|\langle \parallel L + 2S \parallel \rangle|^2$ have been reported by Carnall [22].

The JO theory yields the theoretical oscillator strength of electric dipolar (ED) transitions, $f_{ED, th}$ according to the ex-

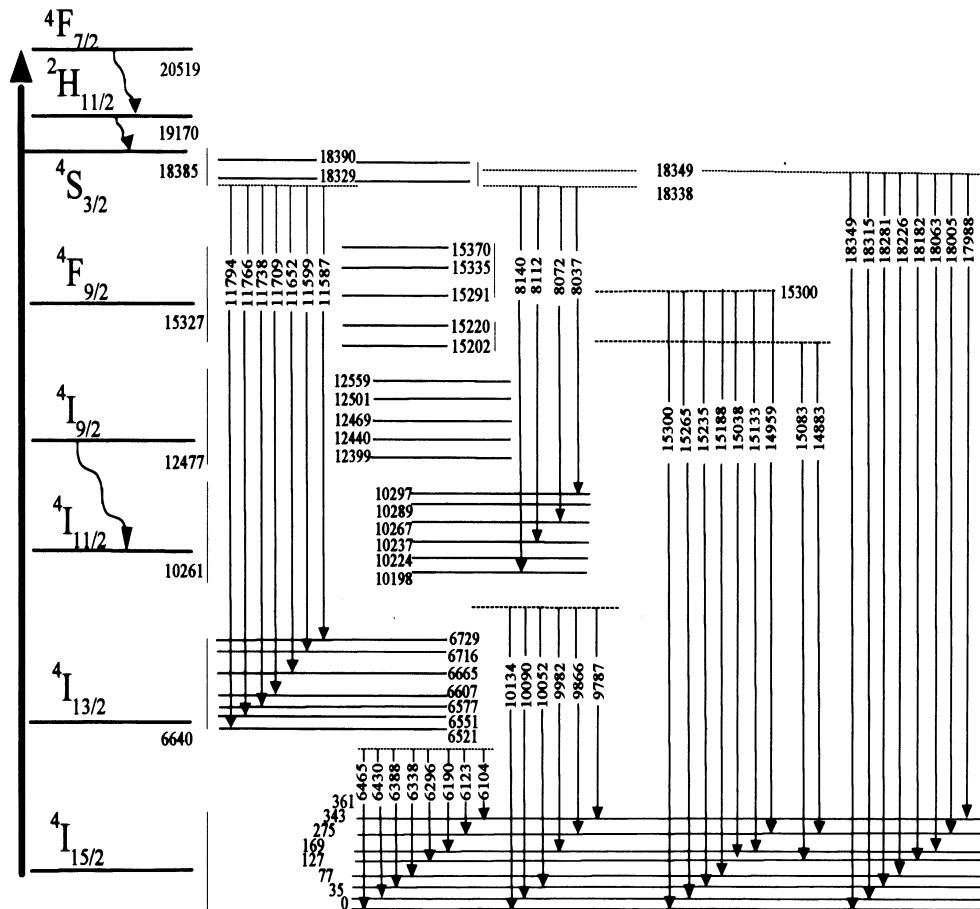**Fig. 4.** Schematic description of the Er^{3+} excitation and photoluminescence emission channels observed in KGW in the 18 450–6060 cm^{-1} spectral range. Energies are given in cm^{-1}

Table 4. Optical absorption bands of Er^{3+} in KGW crystals

$^{2S+1}L_J$ multiplet	$\overline{E}$/cm^{-1} 5 K	Energy of Stark sublevels /cm^{-1} 5 K	FWHM /cm^{-1}	$(\int \alpha \, d\lambda/\rho) \times 10^{28}$ /cm^3 RT	5 K
$^4I_{15/2}$	–	0	–	–	–
		35			
		77			
		127			
		169			
		275			
		343			
		361			
$^4I_{13/2}$	6640	6521	1.3	–	169
		6551	1.5		
		6577	1.9		
		6607	2.5		
		6665	3.1		
		6716	5.3		
		6729	7.2		
$^4I_{11/2}$	10261	10198	1.9	30	33
		10224	3.0		
		10237	3.3		
		10267	3.7		
		10289	4.2		
		10297	12.2		
$^4I_{9/2}$	12477	12399	28.4	–	15
		12440	10.2		
		12469	10.1		
		12501	5.5		
		12559	14.2		
$^4F_{9/2}$	15327	15202	18.6	67	33
		15220	1.6		
		15291	2.8		
		15335	3.4		
		15370	5.5		
$^4S_{3/2}$	18385	18329	2.1	11	3
		18390	3.3		
$^2H_{11/2}$	19170	19053	2.8	410	113
		19074	3.9		
		19143	3.5		
		19181	4.4		
		19215	3.6		
		19226	4.4		
$^4F_{7/2}$	20519	20445	2.4	31	12
		20487	2.8		
		20512	4.0		
		20580	5.1		
$^4F_{5/2}$	22158	22127	2.9	2	3
		22158	2.8		
		22193	3.5		
$^4F_{3/2}$	22518	22473	6.3	–	1
		22559	12.6		
$^2H_{9/2}$	24565	24504	4.1	7	4
		24539	2.7		
		24555	6.0		
		24586	7.9		
		24623	4.4		
$^4G_{11/2}$	26403	26240	3.8	452	123
		26256	4.4		
		26351	6.8		
		26405	9.9		
		26454	0.8		
		26474	8.5		
$^2G_{9/2}$	27348	27309	3.8	–	7
		27322	3.8		
		27348	4.1		
		27373	4.8		
		27388	3.9		

Table 4. *continued*

$^2K_{15/2}$	27773	27431	5.7	–	12
		27524	25.5		
		27608	17.9		
		27660	17.1		
		27750	28.0		
		27823	27.2		
		27948	25.8		
		28006	14.2		

pression

$$f_{ED,th} = \chi \left[\frac{8\pi^2 mc}{h} \right] \frac{1}{3\overline{\lambda}(2J+1)}$$
$$\times \sum_{k=2,4,6} \Omega_k \left| \langle 4f^N \alpha [SL] J \parallel U^\lambda \parallel 4f^N \alpha' \left[S'L' \right] J' \rangle \right|^2, \quad (4)$$

where $\chi = (n^2 + 2)^2 / 9n$, Ω_k are the JO parameters and the reduced matrix elements corresponding to the JJ' transition of Er^{3+}, $\langle \parallel U^\lambda \parallel \rangle$, have been tabulated by Weber [23].

The Ω_k set describing the Er^{3+} spectroscopic properties in KGW has been calculated by minimising the $\sum_{J'} (f_{exp} - f_{ED,th})^2$ differences for the used sample, $N = 1.1 \times 10^{20}$ cm^{-3}. The $f_{ED,th}$ value corresponding to each JJ' multiplet has been calculated using the average refractive index $\overline{n} = 1/2(n_g + n_m)$, where n_g and n_m are obtained from (1) at the corresponding $\overline{\lambda}$ of the multiplet. The quality of the fit is characterised by the root-mean-square (RMS) deviation parameter defined as

$$\mathrm{RMS}(\Delta f) = \left(\frac{\sum_{i=1}^{i=l} (f_{exp} - f_{ED,th})^2}{\text{no. of transitions} - \text{no. of parameters}} \right)^{1/2}. \quad (5)$$

The JO parameters obtained from the fitting procedure are: $\Omega_2 = 8.90 \times 10^{-20}$ cm^2, $\Omega_4 = 0.96 \times 10^{-20}$ cm^2, and $\Omega_6 = 0.82 \times 10^{-20}$ cm^2, $\mathrm{RMS}(\Delta f) = 3.3 \times 10^{-7}$. Table 5 summarises the JJ' transitions used for the calculation, the average wavelengths considered and the difference between the experimental and calculated oscillator strengths. The magnitude of the Ω_k parameters obtained are close to those

Table 5. Room-temperature absorption band positions and electric dipolar oscillator strengths of Er^{3+} in KGW

	$\overline{\lambda}$/nm	$f_{ED,exp} \times 10^6$	$f_{ED,th} \times 10^6$	$|\Delta f| \times 10^6$
$^4G_{11/2}$	380.10	36.12	36.26	0.14
$^2H_{9/2}$	407.74	0.54	0.77	0.23
$^4F_{3/2}$	444.00	-	0.44	-
$^4F_{5/2}$	451.00	-	0.76	-
$^4F_{7/2}$	490.36	1.72	1.98	0.26
$^2H_{11/2}$	524.06	19.20	19.04	0.16
$^4S_{3/2}$	547.98	0.48	0.48	0.00
$^4F_{9/2}$	657.64	1.97	1.94	0.03
$^4I_{9/2}$	801.00	-	0.24	-
$^4I_{11/2}$	977.10	0.24	0.83	0.59
$^4I_{13/2}$	1519.54	1.38	1.24	0.14

obtained for Er^{3+} in the isomorphous $KY(WO_4)_2$ crystals [24] and they are in the range of values expected for Er^{3+} when the two hypersensitive $^4I_{15/2} \rightarrow {}^4G_{11/2}$ and $^2H_{11/2}$ transitions are taken into account [25]. The JO theory has been applied under some simplifications that must be noted: First, a single Er centre has been assumed even though the contributions of multicentres have been suggested for other impurities at concentrations similar to those used in this work [26] and second, the actual anisotropic character of the absorption [27] has been ignored. Despite these simplifications the lifetimes calculated and reported later agree well with those expected for Er^{3+}.

3.3 Photoluminescence

The JO theory also provides a method to evaluate the radiative properties of the rare-earth ions by using the JO parameters, Ω_k, calculated above.

The radiative transition rates, $A_{JJ'}$, for the excited levels are expressed by

$$A_{JJ'} = \chi \left[\frac{32\pi^3 c\alpha_f}{3\overline{\lambda}^3} \right] \frac{n^2}{(2J+1)} \times \sum_{k=2,4,6} \Omega_k \left| \langle 4f^N\alpha[SL]J \parallel U^\lambda \parallel 4f^N\alpha' \left[S'L' \right] J' \rangle \right|^2,$$

(6)

and the magnetic dipolar radiative rates, $A_{MD, JJ'}$, are given by

$$A_{MD, JJ'} = \left[\frac{2\pi\alpha_f h^2}{3m^2 c} \right] \frac{n^3}{(2J+1)\overline{\lambda}^3} \times \left| \langle 4f^N\alpha[SL]J \parallel L+2S \parallel 4f^N\alpha' \left[S'L' \right] J' \rangle \right|^2.$$

(7)

The latter are relevant to describe the emission properties of the $^4I_{11/2} \rightarrow {}^4I_{13/2}$ and $^4I_{13/2} \rightarrow {}^4I_{15/2}$ transitions. The total radiative rate, $A_{JJ'}$, is obtained as the sum of the two contributions above.

Table 6 summarises the radiative transitions calculated for all the Er^{3+} levels with energy equal or lower than the $^2G_{9/2}$ multiplet as well as the luminescence branching ratios defined as

$$\beta_{JJ'} = \frac{A_{JJ'}}{\sum_{J'} A_{JJ'}}$$

(8)

and the radiative lifetimes, τ_{rJ}, given by

$$\tau_{rJ} = \frac{1}{\sum_{J'} A_{JJ'}}.$$

(9)

The erbium photoluminescences have been also characterised experimentally. The unpolarized photoluminescence has been recorded in the 5–300 K temperature range by using the cryostat and the temperature controller described above. The cw spectra have been excited either with the 488 nm emission of an Ar laser or with a Spectra Physics optical parametric oscillation system, model MOPO-730 tuned at 489.1 nm. For wavelengths shorter than 900 nm, the emissions have been analysed by using a Spex 500M ($f = 50$ cm)

Table 6. Spectral average position $\overline{\lambda}$, radiative transition rate $A_{JJ'}$, branching ratio $\beta_{JJ'}$, radiative lifetime τ_r, and experimental lifetime τ_{exp} obtained at room temperature for $[Er] = 1.1 \times 10^{20}$ cm^{-3} in KGW crystals

	$\overline{\lambda}$/nm	$A_{ED, JJ'}$, $A_{MD, JJ'}$/s^{-1}	$\beta_{JJ'}$/%	τ_r/μs	τ_{exp}/μs
$^2G_{9/2} \rightarrow {}^4G_{11/2}$	10 582	0	0.0	27	–
$^2H_{9/2}$	3593	1	0.0		
$^4F_{3/2}$	2070	8	0.0		
$^4F_{5/2}$	1927	64	0.2		
$^4F_{7/2}$	1464	539	1.5		
$^2H_{11/2}$	1223	110	0.3		
$^4S_{3/2}$	1116	36	0.1		
$^4F_{9/2}$	832	1353	3.7		
$^4I_{9/2}$	672	48	0.1		
$^4I_{11/2}$	585	1600	4.4		
$^4I_{13/2}$	483	30 227	82.8		
$^4I_{15/2}$	368	2507	6.9		
$^4G_{11/2} \rightarrow {}^2H_{9/2}$	5441	4	0.0	19	–
$^4F_{3/2}$	2574	1	0.0		
$^4F_{5/2}$	2356	2	0.0		
$^4F_{7/2}$	1700	46	0.1		
$^2H_{11/2}$	1383	18	0.0		
$^4S_{3/2}$	1247	16	0.0		
$^4F_{9/2}$	903	1334	2.6		
$^4I_{9/2}$	718	415	0.8		
$^4I_{11/2}$	620	66	0.1		
$^4I_{13/2}$	506	2881	5.5		
$^4I_{15/2}$	381	48 018	90.9		
$^2H_{9/2} \rightarrow {}^4F_{3/2}$	4885	0	0.0	298	–
$^4F_{5/2}$	4155	0	0.0		
$^4F_{7/2}$	2472	17	0.5		
$^2H_{11/2}$	1854	21	0.7		
$^4S_{3/2}$	1618	0	0.0		
$^4F_{9/2}$	1082	31	0.9		
$^4I_{9/2}$	827	71	2.1		
$^4I_{11/2}$	699	455	13.6		
$^4I_{13/2}$	558	1704	50.9		
$^4I_{15/2}$	407	1048	31.3		
$^4F_{3/2} \rightarrow {}^4F_{5/2}$	27 778	0	0.0	502	–
$^4F_{7/2}$	5003	0	0.0		
$^2H_{11/2}$	2987	0	0.0		
$^4S_{3/2}$	2420	12	0.6		
$^4F_{9/2}$	1391	15	0.7		
$^4I_{9/2}$	996	207	10.4		
$^4I_{11/2}$	816	688	34.5		
$^4I_{13/2}$	630	90	4.5		
$^4I_{15/2}$	448	979	49.2		
$^4F_{5/2} \rightarrow {}^4F_{7/2}$	6101	1	0.1	440	–
$^2H_{11/2}$	3347	3	0.1		
$^4S_{3/2}$	2650	2	0.1		
$^4F_{9/2}$	1464	82	3.6		
$^4I_{9/2}$	1033	111	4.9		
$^4I_{11/2}$	841	83	3.6		
$^4I_{13/2}$	644	892	39.3		
$^4I_{15/2}$	455	1097	48.3		
$^4F_{7/2} \rightarrow {}^2H_{11/2}$	7413	1	0.1	343	–
$^4S_{3/2}$	4686	0	0.0		
$^4F_{9/2}$	1926	8	0.2		
$^4I_{9/2}$	1243	114	4.0		
$^4I_{11/2}$	975	168	5.7		
$^4I_{13/2}$	721	337	11.6		
$^4I_{15/2}$	492	2287	78.4		
$^2H_{11/2} \rightarrow {}^4S_{3/2}$	12 739	0	0.0	76	–
$^4F_{9/2}$	2602	47	0.4		
$^4I_{9/2}$	1494	152	1.2		
$^4I_{11/2}$	1122	85	0.6		
$^4I_{13/2}$	798	157	1.2		
$^4I_{15/2}$	527	12 717	96.6		–

Table 6. *continued*

$^4S_{3/2} \rightarrow {}^4F_{9/2}$	3270	0	0.0	758	27
$^4I_{9/2}$	1693	44	3.3		
$^4I_{11/2}$	1231	27	2.1		
$^4I_{13/2}$	851	350	26.6		
$^4I_{15/2}$	549	896	68.0		
$^4F_{9/2} \rightarrow {}^4I_{9/2}$	3509	7	0.7	886	1
$^4I_{11/2}$	1974	65	5.7		
$^4I_{13/2}$	1151	62	5.5		
$^4I_{15/2}$	660	994	88.1		
$^4I_{9/2} \rightarrow {}^4I_{11/2}$	4513	1	0.5	7900	–
$^4I_{13/2}$	1713	35	27.9		
$^4I_{15/2}$	813	90	71.6		
$^4I_{11/2} \rightarrow {}^4I_{13/2}$	2762	16, 22	20.4	5376	158
$^4I_{15/2}$	992	148	79.6		
$^4I_{13/2} \rightarrow {}^4I_{15/2}$	1548	84, 83	100	5988	–

spectrometer and a GaInAs photomultiplier, and the emissions at wavelengths larger than 900 nm have been recorded by using a Spex 340-E spectrometer ($f = 34$ cm) and a 77 K
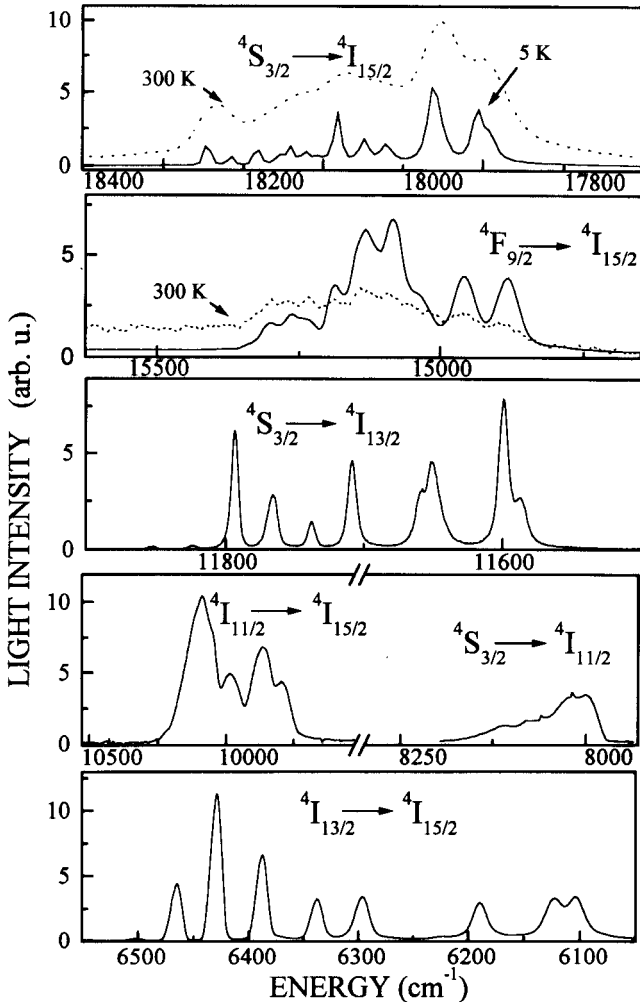

Fig. 5. Overview of the unpolarized photoluminescence of Er^{3+} in KGW single crystals in the $18\,450$–$6060\,cm^{-1}$ spectral range. $[Er] = 1.1 \times 10^{20}\,cm^{-3}$. The spectra have been measured at 5 K (*solid lines*) and 300 K (*dotted lines*)

cooled Ge photodiode. In both cases the detector signals were recorded with a lock-in amplifier.

Figure 5 shows the 5 K unpolarized photoluminescence of Er^{3+} ions in KGW. Up to six luminescence band sets have been observed in the range $18\,450$–$6060\,cm^{-1}$. The incident light used excites electrons to the $^4F_{7/2}$ level (see Fig. 4). Due to the small energy gaps between the $^4F_{7/2}$–$^2H_{11/2}$ levels and the $^2H_{11/2}$–$^4S_{3/2}$ ones ($1219\,cm^{-1}$ and $663\,cm^{-1}$, respectively), the excited electrons decay non-radiatively to the $^4S_{3/2}$ level. From this level, a non-radiative transition to the $^4F_{9/2}$ level takes place as well as further radiative emissions to the $^4I_{9/2}$ or lower energy levels. According to the energy level positions determined by optical absorption, the emission band sets observed in the regions, 8000–8300, 11 500–11 900, and 17 850–18 400 cm^{-1} correspond to $^4S_{3/2} \rightarrow {}^4I_{11/2}$, $^4S_{3/2} \rightarrow {}^4I_{13/2}$, and $^4S_{3/2} \rightarrow {}^4I_{15/2}$ transitions, respectively. Another emission corresponding to the $^4S_{3/2} \rightarrow {}^4I_{9/2}$ may be expected outside of the spectral response of our equipment.

The population of the $^4F_{9/2}$, $^4I_{11/2}$, and $^4I_{13/2}$ levels gives rise to transitions to the ground multiplet, namely $^4F_{9/2} \rightarrow {}^4I_{15/2}$, $^4I_{11/2} \rightarrow {}^4I_{15/2}$, and $^4I_{13/2} \rightarrow {}^4I_{15/2}$ in the 14 700–15 400, 9710–10 260, and 6060–6500 cm^{-1} spectral regions, respectively. The doubled degenerated Stark sublevels of the $^4I_{15/2}$ ground term can be identified in the $^4I_{13/2} \rightarrow {}^4I_{15/2}$ emission. This allows us to quantify the energy position of these sublevels as summarised in Table 4. As was mentioned in the introduction, the $^4I_{13/2} \rightarrow {}^4I_{15/2}$ emission is relevant for optical communication systems. Figure 6 shows the thermal evolution of the latter emission. As the temperature increases more emission peaks appear, mainly due to the thermal population of the $^4I_{13/2}$ sublevels.

Figure 4 also depicts a schematic description of the photoluminescence emission bands observed at 5 K in the present work. A good agreement is generally found between the energy series determined at 5 K by absorption or by photoluminescence, although the most energetic components of the emission series are often found at an energy slightly
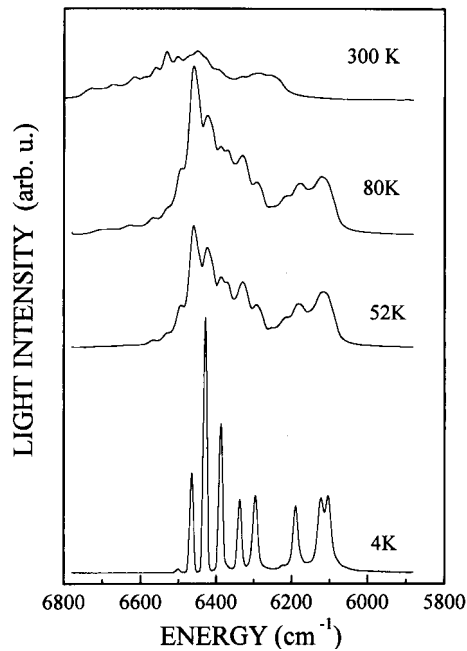

Fig. 6. Thermal evolution of the $^4I_{13/2} \rightarrow {}^4I_{15/2}$ emission of Er^{3+} in KGW

lower $(14–80\,\mathrm{cm^{-1}})$ than that corresponding to absorption. These energy shifts are larger than those that can be attributed to the wavelength calibration of our systems. Maybe, the observed shifts are due to sample heating due to the absorption of the laser light in the cw-photoluminescence experiments.

Lifetime measurements were performed using the MOPO system described above. The photoluminescence decays of $^4S_{3/2}$ and $^4F_{9/2}$ were excited resonantely using $\lambda = 543.8$ nm and $\lambda = 652.1$ nm, respectively, whereas the light decay of the $^4I_{11/2}$ level was observed by exciting the $^4S_{3/2}$ multiplet. According to the results of Table 6, the expected lifetimes of the $^4S_{3/2}$ and $^4F_{9/2}$ multiplets are about one order of magnitude shorter than that corresponding to the $^4I_{11/2}$ multiplet; thus it is expected that the lifetime measurements performed for the $^4I_{11/2}$ multiplet provide a good approximation.

The light intensity decays observed for the $^4S_{3/2}$ and $^4I_{11/2}$ multiplets fit well with a single exponential curve for all the erbium concentrations. Figure 7 shows the room-temperature lifetimes of the $^4S_{3/2}$ and $^4I_{11/2}$ levels obtained as a function of the Er concentration. A reduction of the level lifetime is found with increasing erbium concentration, which shows the presence of energy migration mechanisms. The lifetime measured can be described by

$$\frac{1}{\tau} = \frac{1}{\tau_0} + \frac{1}{\tau_C}, \qquad (10)$$

τ_0 being the lifetime in absence of energy migration and $1/\tau_C$ the probability of energy migration, which is a function of the impurity concentration. From the empirical fits of Fig. 7 we
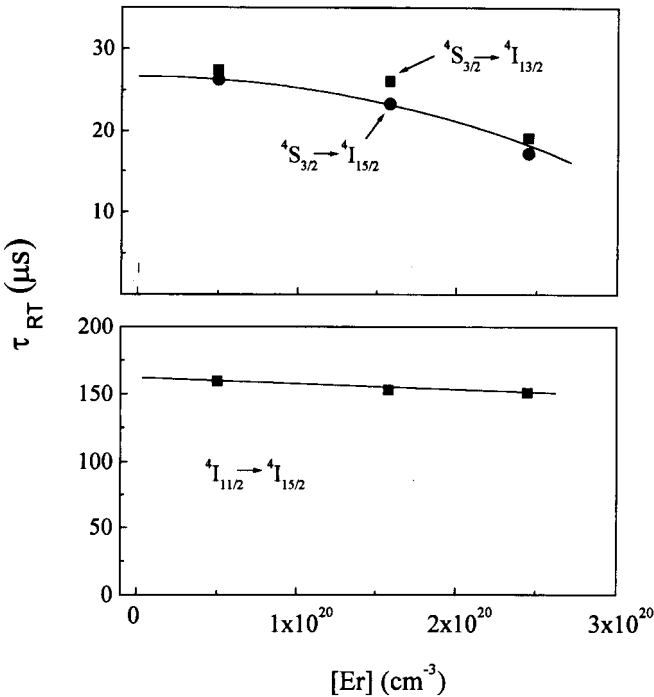
may obtain the room-temperature values, $\tau_0(^4S_{3/2}) = 28\,\mu\mathrm{s}$ and $\tau_0(^4I_{11/2}) = 158\,\mu\mathrm{s}$. These lifetimes are in the order of magnitude observed in other oxides. For instance, the measured lifetime of the $^4I_{11/2}$ level varies from 28 μs in YVO$_4$ to 1.5 ms in Gd$_3$ScGa$_3$O$_{12}$ [2], and that measured for the $^4S_{3/2}$ multiplet in LiNbO$_3$ is 42 μs [4].

The light decays of the $^4F_{9/2}$ multiplet show a peculiar behaviour. The decays observed in samples with the lowest Er concentration can be well analysed by a simple exponential decay, see Fig. 8. The $^4F_{9/2}$ measured lifetime at room temperature is 1.2 μs. However, the light intensity decay of samples with the highest erbium concentration is non-exponential. This can be roughly fitted by using two competitive exponential decays with about 1.8 μs and 19 μs, respectively. This behaviour suggests the presence of a recharging mechanism of the $^4F_{9/2}$ multiplet in the samples with highest erbium concentration.

Up-conversion processes are quite efficient in erbium due to the large number of multiplets available. The excitation with 652.1-nm light populates the $^4I_{11/2}$ multiplet via a non-radiative relaxation [28]. From this level a second photon may be absorbed promoting carriers to the $^2H_{9/2}$ one. Further, at high erbium concentration resonant energy transfer may populate the $^4F_{9/2}$ and higher energy multiplets providing a recharging mechanism of the $^4F_{9/2}$ level, which is suggested to be the origin of the long-lived component in the light decay of the $^4F_{9/2}$ emission.

It is generally observed that the measured lifetimes are lower than the radiative ones calculated by the JO theory. This difference is due to the presence of non-radiative processes, namely multiphonon emissions and energy transfer. As the lifetimes measured in the diluted Er-doped KGW samples are close to the concentration-independent ones, τ_0, we can assume that at this Er concentration the difference is mainly due to multiphonon emission processes, therefore $\tau_{\mathrm{exp}}^{-1} = \tau_r^{-1} + \tau_{\mathrm{ph}}^{-1}$, where τ_{ph}^{-1} is the multiphonon relaxation rate. Following the phenomenological model of Riseberg and Moos [29] the temperature dependence of the multiphonon
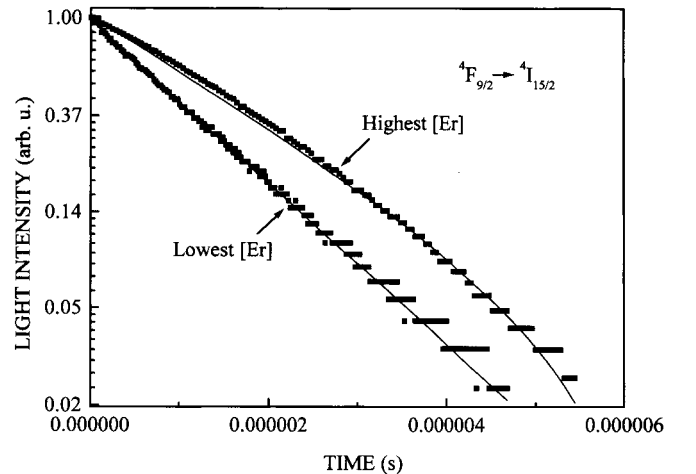

Fig. 7. Room-temperature lifetimes of Er^{3+} in KGW crystals as a function of the erbium concentration calculated by EPMA. $^4S_{3/2}$; $\lambda_{\mathrm{exc}} = 543.8$ nm, $\lambda_{\mathrm{emi}} = 558$ nm for $^4I_{15/2}$, and $\lambda_{\mathrm{emi}} = 862$ nm for $^4I_{13/2}$ transitions. $^4I_{11/2}$ to $^4I_{15/2}$ emission, $\lambda_{\mathrm{exc}} = 543.8$ nm, $\lambda_{\mathrm{emi}} = 980$ nm. The *lines* are empirical fits of the experimental values

Fig. 8. Light intensity decays of the $^4F_{9/2} \rightarrow {}^4I_{15/2}$ emission for lowest and highest erbium concentrations used. The *straight line* in the lowest Er concentration is the fit obtained with a single exponential, and in the upper Er concentration the fit corresponds to the competition of two exponential decays
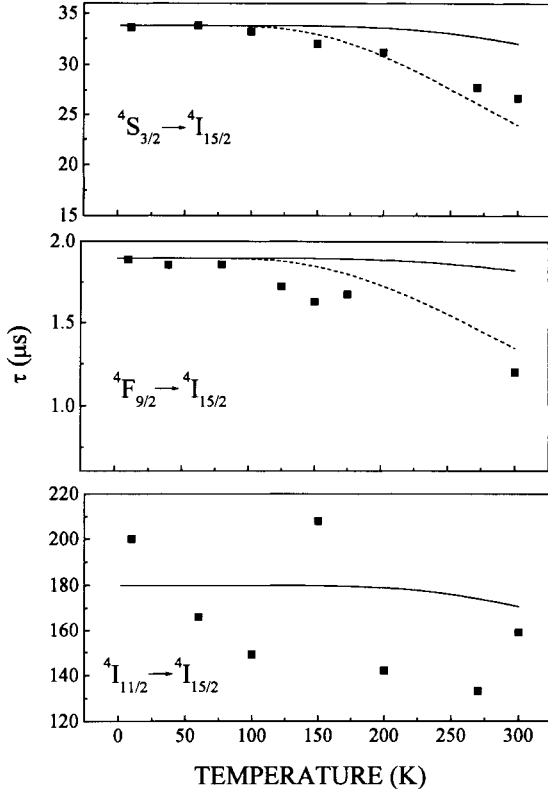
Fig. 9. Temperature dependence of the erbium lifetimes for several emission bands. $[Er] = 1.1 \times 10^{20}$ cm^{-3}. The *continuous lines* are the fits obtained using (11) and a phonon energy of 901 cm^{-1}. The *dashed lines* are the fits obtained assuming the simultaneous contribution of 901 cm^{-1} ($p = 1$) and 528 cm^{-1} ($p' = 4$) phonons

relaxation rate is given by

$$\tau_{ph}^{-1}(T) = \tau_{ph}^{-1}(0)(1+n)^p \tag{11}$$

where $n = 1/\left[\exp\left(\overline{h}\omega/kT\right) - 1\right]$, $\overline{h}\omega$ being the energy of the phonon emitted, k the Boltzmann constant and p the number of phonons required to maintain the energy conservation in a non-radiative transition between the levels separated by ΔE.

Figure 9 shows the lifetime temperature dependence of the $^4S_{3/2}$, $^4F_{9/2}$, and $^4I_{11/2}$ levels in samples with the lowest erbium concentration. The lifetimes obtained decrease with increasing temperature. Figure 9 also shows (continuous line) the fit obtained using (11) and assuming the emission of four phonons ($p = 4$) with the largest energy, namely 901 cm^{-1} [13]. Despite the large uncertainty in the experimental determination of the $^4I_{11/2}$ lifetimes, the temperature dependence obtained from the fit agrees well with the experimental results. However, the temperature dependences obtained for the $^4F_{9/2}$ and $^4S_{3/2}$ multiplets do not fit well the behaviour of the measurements. In these cases the simultaneous emission of phonons with lower energy is often assumed and the multiphonon relaxation rate is accounted by [4, 30]

$$\tau_{ph}^{-1}(T) = \tau_{ph}^{-1}(0)(1+n)^p(1+n')^{p'}. \tag{12}$$

The dashed lines of Fig. 9 show the fits obtained assuming the simultaneous emission of 901 cm^{-1} ($p = 1$) and
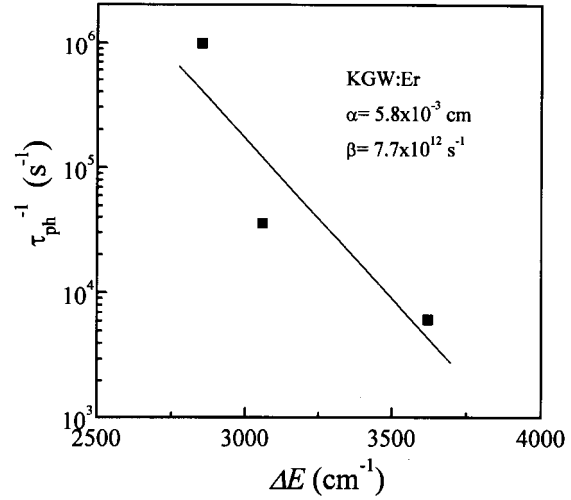

Fig. 10. Non-radiative multiphonon transition rates at 5 K of Er^{3+} in KGW as a function of the energy distance to the nearest lower level. $[Er] = 1.1 \times 10^{20}$ cm^{-3}. The *line* is the best fit obtained

528 cm^{-1} ($p' = 4$) phonons observed in the Raman spectrum of KGW. It must be also noted that for the $^4S_{3/2}$ level, the thermal population of the $^2H_{11/2}$ multiplet may also contribute to the temperature dependence of the non-radiative relaxation.

The quantum efficiency of the luminescence at 5 K, $\eta = \tau_{exp}/\tau_r$, can be estimated from Fig. 9 as 4.5%, 0.1%, and 2.9% for the $^4S_{3/2}$, $^4F_{9/2}$, and $^4I_{11/2}$ multiplets, respectively. At low temperature, (11) can be approximated as $\tau_{ph}^{-1} = \beta \exp(-\alpha\Delta E)$, where α and β depend on the host but not on the rare-earth ion and ΔE is the energy difference between the excited level and the next lower-lying level. Figure 10 shows a fit of τ_{ph}^{-1} versus ΔE. The characteristic values obtained for the KGW host are $\alpha = 5.8 \times 10^{-3}$ cm and $\beta = 7.7 \times 10^{12}$ s^{-1}.

4 Conclusions

It has been shown that the growth of KGW doped with Er^{3+} is possible from K$_2$W$_2$O$_7$ flux using TSSG technique. The distribution coefficient of erbium in KGW is 0.8. The principal axis with highest refractive index, n_g, lies in the (010) plane at 21.5° of the crystallographic c axis. The optical absorption bands of Er^{3+} in KGW crystals measured at 5 K show the $(2J+1)/2$ splitting expected in the C$_2$ local symmetry at the gadolinium site of the lattice. The energy position and absorption cross sections of the different optical absorption multiplets have been characterised as well as the luminescence channels of Er^{3+} in the 6060–18 450 cm^{-1} region. The room-temperature absorption and photoluminescence have been described in the framework of the Judd–Ofelt theory. The comparison between the radiative lifetimes calculated and those measured show the relevance of non-radiative processes in KGW.

References

1. J.L. Doulajan, P. Leboulanger, S. Girard, J. Margerie, F.S. Ermeneux, R. Moncorge: J. Luminesc. **72-74**, 179 (1997)
2. S.A. Payne, L.K. Smith, W.F. Krupke: J. Appl. Phys. **77**, 4274 (1995)
3. J. Amin, B. Dussardier, T. Schweizer, M. Hemsptead: J. Luminesc. **69**, 17 (1996)
4. L. Nuñez, G. Lifante, F. Cussó: Appl. Phys. B **62**, 485 (1996)
5. A.A. Kaminskii: Ann. Phys. Fr. **16**, 639 (1991)
6. M. Bass, W.Q. Shi, R. Kurtz, M. Kokta, H. Diegl: In *Tunable Solid State Lasers II*, ed. by A.B. Budgor, L. Esterowitz, L.G. DeShazer (Springer, Berlin, Heidelberg 1986) pp. 300–305
7. N.V. Kuleshov, A.A. Lagatsky, V.G. Shcherbitsky, V.P. Mikhailov, E. Heumann, T. Jensen, A. Diening, G. Huber: Appl. Phys. B **64**, 409 (1997)
8. A. Kaminskii, L. Li, A.V. Butashin, V.S. Mironov, A.A. Pavlyuk, S.N. Bagayev, K. Ueda: Jpn. J. Appl. Phys. **36**, L107 (1997)
9. A.A. Kaminskii: *Crystalline Lasers: Physical Processes and Operating Schemes* (CRC Press, BocaRaton, New York, London, Tokyo 1996) p. 185
10. A.A. Kaminskii, A.A. Pavlyuk, T.I. Butaeva, V.A. Fedorov, I.F. Balashov, V.A. Berenberg, V.V. Lyubchenko: Neorg. Mat. **13**, 1541 (1977)
11. V. Kushawaha, A. Banerjee, L. Major: Appl. Phys. B **56**, 239 (1993)
12. Y. Chen, L. Major, V. Kushawaha: Appl. Opt. **35**, 3203 (1996)
13. I.V. Mochalov: J. Opt. Technol. **62**, 746 (1995)
14. R. Solé, V. Nikolov, X. Ruiz, Jna. Gavalda, X. Solans, M. Aguiló, F. Díaz: J. Cryst. Growth **169**, 600 (1996)
15. S.V. Borisov, R.F. Klevtsova: Sov. Phys. Crystall. **13**, 420 (1968)
16. P.V. Klevtsov, L.P. Kozeeva: Sov. Phys. Doklady **14**, 185 (1969)
17. *International Tables for Crystallography*, Vol. A., 3rd edn., ed. by T. Hanh, for the IUCr by D. Reidel Pu. Company., 1992
18. T. Graf, J.E. Balmer: Opt. Eng. **34**, 2349 (1995)
19. G.V. Ananieva, I.I. Afanasiev, V.I. Vasilieva, A.I. Glazon, I.Ya. Mamontov, T.I. Merkulyaeva: Opt. Mekt. Promst. **8**, 35 (1983)
20. B.R. Judd: Phys. Rev. **127**, 750 (1962)
21. G.S. Ofelt: J. Chem. Phys. **37**, 511 (1962)
22. W.T. Carnall, P.R. Fields, B.G. Wybourne: J. Chem. Phys. **42**, 3797 (1965)
23. M.J. Weber: Phys. Rev. B **157**, 262 (1967)
24. N.V. Kuleshov, A.A. Lagatsky, A.V. Podlipensky, V.P. Mikhailov, A.A. Kornienko, E.B. Dunina, S. Hartung, G. Huber: J. Opt. Soc. Am. B **15**, 1205 (1998)
25. R.D. Peacock: Chem. Phys. Lett. **16**, 590 (1972)
26. J. Ripoll, L.E. Bausá, C. Terrile, J. García Solé, F. Díaz: J. Luminesc. **72**/**74**, 253 (1997)
27. A.A. Kaminskii, S.E. Sarkisov, A.A. Pavlyuk, V.V. Lyubchenko: Neorg. Mat. **16**, 720 (1980)
28. T. Danger, J. Koetke, R. Brede, E. Heumann, G. Huber, B.H.T. Chai: J. Appl. Phys. **76**, 1413 (1994)
29. L.A. Riseberg, H.W. Moss: Phys. Rev. **174**, 429 (1968)
30. E.D. Reed, H.W. Moos: Phys. Rev. B **8**, 980 (1973)